International Journal of Fatigue 31 (2009) 1176–1189

Contents lists available at ScienceDirect

International Journal of Fatigue

journal homepage: www.elsevier.com/locate/ijfatigue

3D modeling of subsurface fatigue crack nucleation potency of primary inclusions in heat treated and shot peened martensitic gear steels

Rajesh Prasannavenkatesan [a], Jixi Zhang [c], David L. McDowell [a,b,*], Gregory B. Olson [d,e], Herng-Jeng Jou [e]

[a] George W. Woodruff School of Mechanical Engineering, Georgia Institute of Technology, Atlanta, GA 30332-0405, USA
[b] School of Materials Science and Engineering, Georgia Institute of Technology, Atlanta, GA 30332-0245, USA
[c] Department of Mechanical Engineering, University of Nevada, Reno, NV 89557, USA
[d] Department of Materials Science and Engineering, Robert R. McCormick School of Engineering and Applied Science, Northwestern University, Evanston, IL 60208-3108, USA
[e] Questek Innovations LLC, Evanston, IL 60201, USA

ARTICLE INFO

Article history:
Received 29 July 2008
Received in revised form 25 November 2008
Accepted 3 December 2008
Available online 13 December 2008

Keywords:
Shot peening
Residual stress
3D finite element analysis
Fatigue crack nucleation
Subsurface cracking
Inclusions

ABSTRACT

A computational strategy is developed to characterize the driving force for fatigue crack nucleation at subsurface primary inclusions in carburized and shot peened C61® martensitic gear steels. Experimental investigation revealed minimum fatigue strength to be controlled by subsurface fatigue crack nucleation at inclusion clusters under cyclic bending. An algorithm is presented to simulate residual stress distribution induced through the shot peening process following carburization and tempering. A methodology is developed to analyze potency of fatigue crack nucleation at subsurface inclusions. Rate-independent 3D finite element analyses are performed to evaluate plastic deformation during processing and service. The specimen is subjected to reversed bending stress cycles with $R = 0.05$, representative of loading on a gear tooth. The matrix is modeled as an elastic–plastic material with pure nonlinear kinematic hardening. The inclusions are modeled as isotropic, linear elastic. Idealized inclusion geometries (ellipsoidal) are considered to study the fatigue crack nucleation potency at various subsurface depths. Three distinct types of second-phase particles (perfectly bonded, partially debonded, and cracked) are analyzed. Parametric studies quantify the effects of inclusion size, orientation and clustering on subsurface crack nucleation in the high cycle fatigue (HCF) or very high cycle fatigue (VHCF) regimes. The nonlocal average values of maximum plastic shear strain amplitude and Fatemi–Socie (FS) parameter calculated in the proximity of the inclusions are considered as the primary driving force parameters for fatigue crack nucleation and microstructurally small crack growth. The simulations indicate a strong propensity for crack nucleation at subsurface depths in agreement with experiments in which fatigue cracks nucleated at inclusion clusters, still in the compressive residual stress field. It is observed that the gradient from the surface of residual stress distribution, bending stress, and carburized material properties play a pivotal role in fatigue crack nucleation and small crack growth at subsurface primary inclusions. The fatigue potency of inclusion clusters is greatly increased by prior interfacial damage during processing.

1. Introduction

Although much progress has been made, development of quantitative descriptions of potency of primary inclusions for fatigue crack nucleation and early stages of growth in high strength steels requires further understanding to support quantitative materials design. Carburization and shot peening are well established techniques for improving high cycle fatigue strength of steel components [1–7]. The fact that bending fatigue strength of steel gear teeth is increased considerably by carburization and shot peening has been extensively utilized in industry [8–11]. With carburization and shot peening, crack initiation (nucleation and early growth at the scale of the primary inclusion) is observed to shift from the surface toward the subsurface of the carburized gears; this is primarily due to presence of high compressive residual stress and comparatively high hardness at the surface. It is widely observed that cracks in unnotched specimens nucleate at nonmetallic inclusions and other microstructure inhomogeneities. Such second-phase particles often serve as fatigue crack starters in a variety of metallic materials [12–18]. Extensive experimental observations have been reported earlier on subsurface crack initiation [19–23].

Toyada et al. [21] performed a series of rotating-bending fatigue tests on Cr–Mo steels and estimated the influence of the inclusions on the fatigue strength by employing the projected $\sqrt{\text{area}}$

* Corresponding author. Address: George W. Woodruff School of Mechanical Engineering, Georgia Institute of Technology, Atlanta, GA 30332-0405, USA; Tel.: +1 404 894 5128; fax: +1 404 894 0186.
E-mail address: david.mcdowell@me.gatech.edu (D.L. McDowell).

0142-1123/$ - see front matter © 2008 Elsevier Ltd. All rights reserved.
doi:10.1016/j.ijfatigue.2008.12.001

Nomenclature

σ_{ys}	uniaxial cyclic yield strength	$\dot{\bar{\varepsilon}}^p$	equivalent plastic strain rate
σ_{ij}	stress tensor components	σ^{res}	residual stress magnitude
ε_{ij}	strain tensor components	ε_a	applied strain amplitude
S_{ij}	deviatoric stress tensor components	E	Young's modulus
σ^h	hydrostatic stress	ν	Poisson's ratio
α_{ij}	back stress tensor components	γ	engineering shear strain
$\bar{\sigma}$	Mises uniaxial effective stress	$\Delta\gamma^{p^*}_{\max}$	nonlocal maximum plastic shear strain range
α'_{ij}	deviatoric back stress tensor components	$\Delta\Gamma$	Fatemi–Socie (FS) parameter
α^h	hydrostatic part of the back stress tensor	$\sigma^n_{\max}$	maximum stress normal to plane of maximum shear strain range in a loading cycle
$\dot{\underset{\sim}{\varepsilon}}^e$	elastic strain rate tensor		
$\dot{\underset{\sim}{\varepsilon}}^p$	plastic strain rate tensor		

approach suggested by Murakami and Endo [13], with necessary modifications to incorporate the residual stress effects. They argued that there exists a critical inclusion size that initiates subsurface fatigue failure within the specimen. The semi-empirical Murakami and Endo model has successfully predicted upper and lower bounds on service lives for specimens containing inclusions. The fracture mechanics approach has also been widely applied for bending fatigue analysis of carburized steel components [24–26]. Kim and co-workers [24] studied the effect of surface residual stress on fatigue life by analyzing the change in stress intensity factor due to residual stress. Sharma and co-workers [25] presented a detailed study of various factors influencing K_{1c} of case steels including alloying elements, retained austenite and carbon content. Lin et al. [26] investigated the general methodology of bending fatigue life prediction using strain-life and linear elastic fracture mechanics (LEFM) approaches for SAE 8620 steel. Both approaches were reported to predict the fatigue lives very well, although the strain-life approach proved to be more conservative in its predictions. Life prediction schemes based on nominal strain-life or LEFM are insufficient to fully reflect the mechanisms for crack nucleation at non-metallic inclusions; as such, they cannot serve to quantify the microstructure-level details of threshold condition on cyclic stress amplitude to form a fatigue crack which can propagate away from the inclusion. More detailed analyses of the inclusion size and shape, interface characteristics, local residual stresses, contrast of elastic and thermal properties, and even surrounding microstructure of the matrix are necessary to explore this issue in more detail.

Mackaldener and co-workers [27] developed a two-dimensional plane strain gear tooth FE model and studied the stress state history at every point within the tooth during a single contact load cycle. The residual stress induced through case hardening was simulated by applying a thermal load cycle and the McDiarmid critical plane approach [28] was employed to predict fatigue crack initiation at various depths with necessary modifications to incorporate shot peening effects. They reported that the tensile residual stresses due to case hardening led to high risk of fatigue crack initiation in the interior of the tooth. Although the method was effective computationally and considered various aspects of surface treatment in the macroscopic analysis, it was not able to describe the root cause for subsurface crack initiation where the residual stresses are still compressive and the role of microstructural inhomogeneity in such failure scenarios. Borbeley et al. [29] attempted to study the cause for subsurface failures initiating from pores in AZ91 magnesium alloys through 3D FE simulations. Results of local stresses and plastic strains in the vicinity of the pores showed a critical size for pores just beneath the surface with a maximum tendency to initiate cracks. Wang and co-workers [16] developed a deterministic model to correlate the total fatigue life and subsurface failure for six different ultra-high strength steels. Although the method was successful in obtaining a good correlation between inclusion size and fatigue life, it is insufficient to address many other factors which play a pivotal role, e.g., particle clustering, orientation with respect to principal stresses, and residual stresses.

Residual stresses play a pivotal role in affecting crack initiation and propagation. Considerable effort has been made to accurately model the residual stresses and account for their influence on service life of the component [30–37]. Some previous work has considered the effects of damaged particles or inclusions on fatigue crack formation and early growth in the micronotch root field of cracked or debonded inclusions [17,18,38–41]. As mentioned above, a simple assumption that fatigue cracks form immediately at such inclusions as a precursor to application of LEFM ignores the complexities of the details of inclusion geometry, damage state, interface condition, and microstructure, all of which can play a role in the near-threshold regime of fatigue strength of these materials. This is important for HCF or very high cycle fatigue (VHCF) applications.

In support of a new generation of high fidelity materials design tools, the aim of the present work is to develop a 3D modeling strategy for a comparative parametric study of the potency for nucleation of fatigue cracks at damaged primary inclusions in carburized and shot peened martensitic gear steels. Specific attention is devoted to the case of Al_2O_3 inclusions in carburized and shot peened C61 alloy gear steel [42]. A new algorithm is presented to model representative residual stresses induced via plastic deformation due to shot peening. Case hardening (carburization and tempering) is considered by varying the material properties from surface to core. To determine quantitative relationships between local plastic strains and far-field loading, representative 3D finite element meshes are constructed which contain inclusions surrounded by carburized matrix. Both cracked and debonded inclusions are considered, consistent with experimental findings. We focus on processes of crack formation and early growth in the matrix under the influence of the strain concentration of the inclusion notch root field, and do not include the fracture mechanics problem of physically small and long crack growth away from the particle. The former (nucleation and early growth) establish the crack origin and often a majority of the fatigue life in HCF and VHCF. We define nucleation as the formation of a crack within the matrix in the region of highest cyclic plastic strain localization near the matrix–inclusion interface; this is considered heuristically as a zone of subcritical crack formation and growth to a stable nucleus that would be amenable to propagation analysis via fracture mechanics.

Relative fatigue crack nucleation potency at various case depths is compared with experimental findings regarding subsurface depths at which cracks form. Nonlocal average values of plastic shear strain range [18,38,41] and the Fatemi–Socie parameter [43] are considered as the candidate driving forces for fatigue crack nucleation. All simulations were performed using the ABAQUS [44] finite element code.

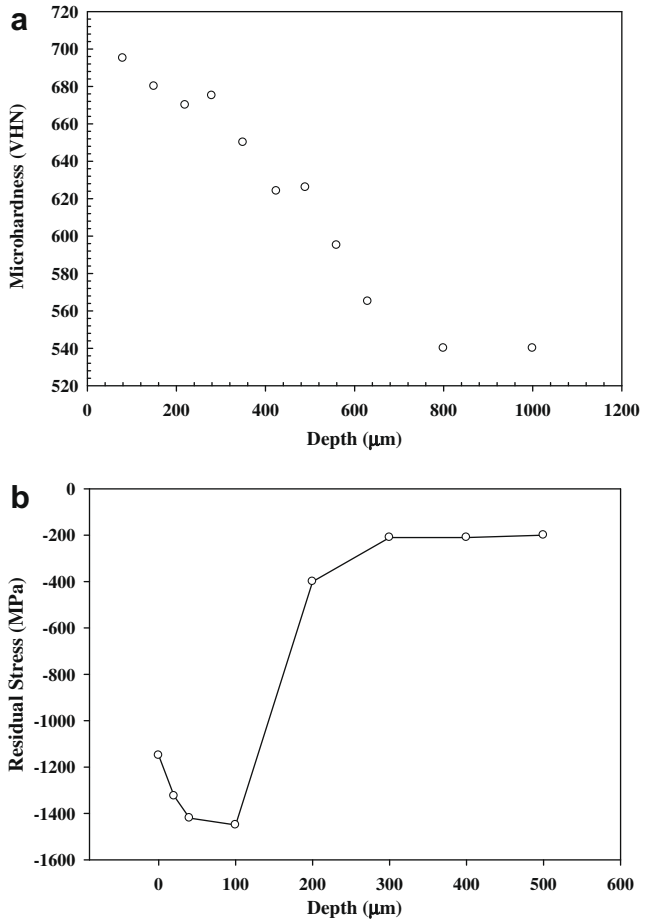

Fig. 1. Measured hardness and residual stress profiles [1]: (a) variation of Vickers microhardness after heat treatment (carburization and tempering) with depth and (b) variation of residual stress with depth after shot peening.

2. Experimental observations of fatigue in case hardened steel

The material of investigation is commercial C61 high-performance gear steel subjected to carburization, tempering and shot peening. This is a martensitic steel with predominantly tempered lath martensite microstructure as confirmed by X-ray diffraction. The experimentally measured profiles of microhardness after heat treatment and residual stress distribution after shot peening are shown in Fig. 1a and b, respectively [1]. Microhardness measurements were made using Buehler Micromet II Micro Hardness Tester following ASTM standard E92 [45]. Prior to measurement, specimens were mounted in Bakelite and then ground and polished up to 1 μm finish. The procedure to measure the residual stress profile following shot peening is explained elsewhere [46]. With the increase of case depth, the carbon content decreases, as does the microhardness. As measured by X-ray diffraction, initial compressive residual stress exists after shot peening within a thickness of 0.5 mm in the surface layer and reaches a maximum value of −1400 MPa at a depth of around 75–100 μm. Under reversed bending stress with $R = 0.05$, it is observed that fatigue cracks defining minimum properties form at a depth of approximately 200–270 μm below surface (Fig. 2a) in spur gear teeth. Similar observations on subsurface fatigue crack initiation have been reported earlier by Shiozawa and Lu [23]. Scanning electron microscopy (SEM) was employed to characterize the fracture surface of failed spur gear teeth as well as the topography and features of various spur gear surface conditions. A Hitachi S-3500 microscope with tungsten hairpin filament was used with a 20 kV electron beam while the specimen chamber maintained a vacuum level of 10^{-4} torr. A secondary electron detector was used to image topographic features while a backscatter electron detector was used to achieve chemical contrast of inclusion phases located on fracture surfaces. Qualitative chemical analysis and mapping of inclusion phases was performed using a PGT energy dispersive X-ray analyzer. The site of crack nucleation is not in the tensile residual stress region. Analysis of the fracture surface and its mating surface indicates that the cracks are formed at clusters of inclusions.

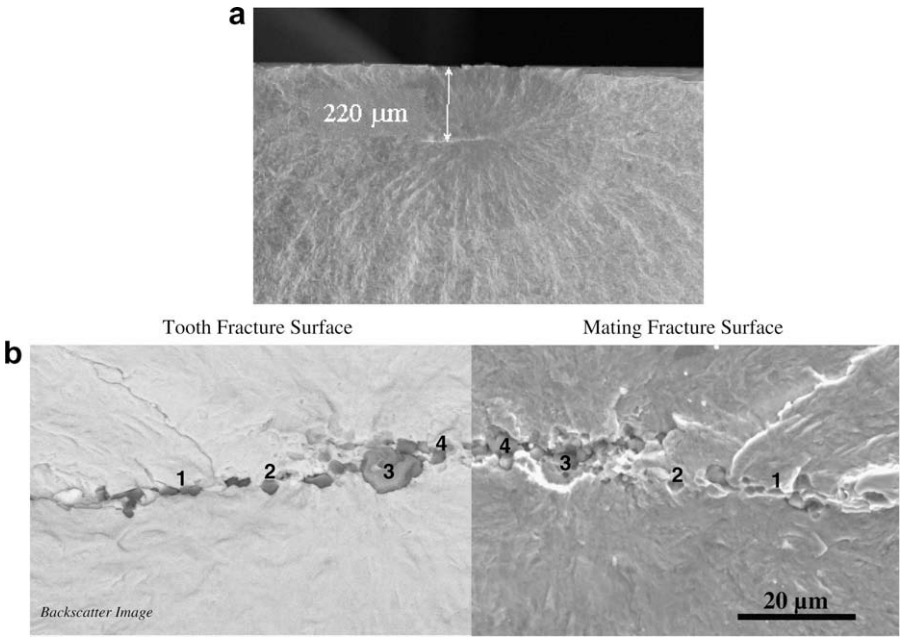

Fig. 2. (a) SEM micrograph of fracture surface indicating the depth of fatigue crack origin and (b) backscatter SEM image of crack initiation zone showing characteristic inclusion sizes, clustering and debonding of inclusion-matrix interfaces [1].

A single row of Al_2O_3 inclusions (particle 1,2,3 &4) on the tooth fracture surface and the corresponding location of cavities on the mating surface are shown for clarity in Fig. 2b [1]. The large particle (#3), about 10 μm in size, could be the favorable site for fatigue crack nucleation [13]. Debonding of particles was observed, with uncracked particles on the fracture surface and corresponding cavities on the mating surface. Inclusion clustering observed at the initiation site indicates a potential role for inclusion interaction. Furthermore, the variation in material properties, distribution of residual stress, and magnitude and gradient of applied stress affect the fatigue crack nucleation process in the subsurface in a cooperative manner. The aforementioned brief introduction of the essential experimental results on microhardness, XRD residual stress measurements, fatigue tests, and SEM micrographs of fracture surface should suffice to convey the problem we intend to address.

3. Characterization of mechanical properties of matrix and inclusions

Three-dimensional FE analyses were performed to understand the mechanisms of fatigue crack nucleation within the tempered martensite matrix. Detailed description of heat treatment, surface treatment and composition of the material is presented by Tiemens [1,2]. The inclusions were assumed to be isotropic linear elastic with Young's modulus $E = 400$ GPa and Poisson's ratio $\nu = 0.2$. The matrix was modeled as a rate-independent elastic-plastic material with a nonlinear kinematic hardening law cast in a format of hardening with dynamic recovery. The variation of carbon content from the surface to core following carburization has significant influence on local mechanical properties of the material. Elastic modulus, yield strength and work hardening rate depend on carbon content. Donzella et al. [47] and Pedersen et al. [48] presented an empirical relation between yield strength and microhardness for case hardened steel. However, for carbon steel subjected to cyclic loading, softening occurs and thus the yield strength may be scaled down by 15–35% from the initial value [49]. Considering the experimental observations and applying the empirical relations, the material parameters of C61 steel were estimated for purposes of FE analyses. It is acknowledged that an accurate measurement of material property gradients in the carburized layer is tedious; in view of the desire to account for the effect of carburization we adopt the aforementioned strategy. In this work, we present some primary results and focus more on the development of the methodology. The variations of material parameters with depth adopted in the current investigation are listed in Table 1. Fig. 3 shows the simulated monotonic tension stress–strain curves at various depths for the material considered.

Table 1
Variation of material properties with the depth from surface.

Depth (m)	E (MPa)	$_{ys}$ (MPa)	c (MPa)	r
0 (Surface)	193,000	998	112,000	200
110	193,550	970	112,428	200
150	193,750	942	113,083	200
170	193,850	927	113,517	200
190	193,950	912	114,018	200
200	194,000	904	114,292	200
220	194,100	890	114,883	200
250	194,250	867	115,872	200
275	194,375	860	116,780	200
300	194,500	850	117,756	200
325	194,625	840	118,790	200
350	194,750	830	119,875	200
1000 (core)	198,000	800	120,000	200

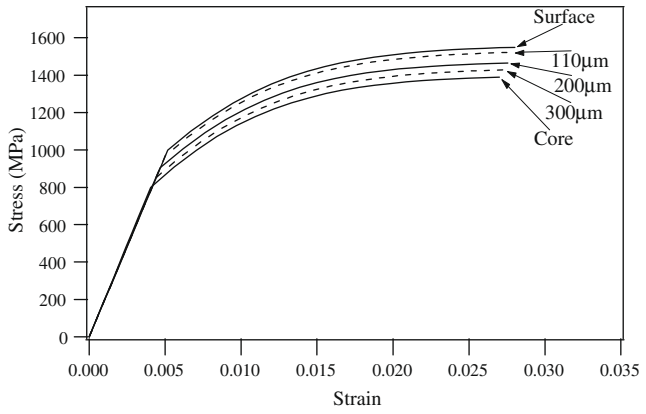

Fig. 3. Simulated monotonic tension stress–strain curves as a function of depth from surface. Depth of core is 1.0 mm below surface.

4. General outline of elasto-plastic framework

The rate-independent plasticity model with combined kinematic-isotropic hardening for the matrix is based on the simple Mises yield surface

$$F = f(\underset{\sim}{\sigma} - \underset{\sim}{\alpha}) - \sigma_{ys}^2 \tag{1}$$

with $F = 0$ during plastic flow. Here, σ and α are the stress and back stress tensors, respectively, and σ_{ys} is the uniaxial yield strength. The function f in Eq. (1) is defined by

$$f(\underset{\sim}{\sigma} - \underset{\sim}{\alpha}) = \frac{3}{2}(\underset{\sim}{S} - \underset{\sim}{\alpha'}) : (\underset{\sim}{S} - \underset{\sim}{\alpha'}) = \frac{3}{2}(S_{ij} - \alpha'_{ij})(S_{ij} - \alpha'_{ij}) \tag{2}$$

The associative plastic flow rule is given by

$$\dot{\underset{\sim}{\varepsilon}}^p = \sqrt{\frac{3}{2}}\dot{\bar{\varepsilon}}^p \frac{\partial F}{\partial \underset{\sim}{\sigma}} \left\| \frac{\partial F}{\partial \underset{\sim}{\sigma}} \right\|^{-1} = \sqrt{\frac{3}{2}}\dot{\bar{\varepsilon}}^p \underset{\sim}{N} = \sqrt{\frac{3}{2}}\dot{\bar{\varepsilon}}^p \frac{(S_{ij} - \alpha'_{ij})}{||(S_{ij} - \alpha'_{ij})||} \tag{3}$$

where $\dot{\bar{\varepsilon}}^p$ is defined by

$$\dot{\bar{\varepsilon}}^p = \sqrt{\frac{2}{3}\dot{\underset{\sim}{\varepsilon}}^p : \dot{\underset{\sim}{\varepsilon}}^p} \tag{4}$$

The evolution equation for the back stress tensor α is expressed as [50]

$$\dot{\underset{\sim}{\alpha}} = \frac{c}{\sigma_{ys}}(\underset{\sim}{\sigma} - \underset{\sim}{\alpha})\dot{\bar{\varepsilon}}^p - r\,\underset{\sim}{\alpha}\,\dot{\bar{\varepsilon}}^p \tag{5}$$

where c and r are material parameters. Here, c is the initial kinematic hardening modulus and r determines the rate of dynamic recovery of the back stress with increasing plastic deformation. Isotropic hardening is neglected in view of the desire to simulate cyclically stable response in parametric studies with pure kinematic hardening. The elastic response is given by

$$\underset{\sim}{\sigma} = \underset{\sim}{C} : \underset{\sim}{\varepsilon}^e \tag{6}$$

where ε^e denotes the elastic strain tensor and C is the isotropic elastic stiffness tensor.

5. Imposition of initial residual stress: modeling the effect of shot peening process

During processing, heat treatment (carburization and tempering) and surface treatment (shot peening) introduce a lateral compressive residual stress field at and near the surface. Comparatively, the residual stress introduced by carburization and tempering (−100 MPa to −300 MPa) is much less than that

introduced through shot peening, especially close to the surface layer of the specimen [1,51]. A series of nonequilibrium thermo-mechanical processes, such as diffusion, temperature-induced phase transformation, dynamic elastic–plastic deformation, and deformation-induced phase transformation are potentially involved during carburization, tempering and shot peening. As a result, it is very complex to simulate the evolution of residual stress based on the physical mechanisms. Although mechanism-based FE simulation of residual stress is effective for two-dimensional calculations, three-dimensional simulations become computationally more demanding. Alternatively, a simplified scheme is followed to impose the residual stresses.

After carburization, the mechanical properties vary only with the depth. Kobayashi and co-workers [52] considered that the shot peening process effectively induces equi-biaxial residual compressive stresses within the specimen by virtue of plastic deformation. It is reasonable to assume that the residual stress in the steel matrix near the surface after shot peening is also equi-biaxial; of course, very near the surface the material may undergo tribological transformation (phase transformation, extensive shear, refinement of structure, etc.), but this zone is typically small (<30 μm or so) compared to the depths at which fatigue cracks form. Fig. 4a shows a schematic of the shot peening process. Fig. 4b shows an equivalent volume element of the plastic zone (subsurface affected by shot peening) divided into multiple 'subsurface elements', each corresponding to a depth *d* below surface. The residual elastic strains in the subsurface correspond to a self-equilibrating residual stress field, with compression near the surface and a tensile stress state deeper into the subsurface. During shot peening the principal stress components are compressive. With these observations and idealizations, a methodology is developed to simulate residual stresses within the material induced by shot peening with respect to the surface coordinate system *XYZ* (Fig. 5). The procedure is summarized as follows:

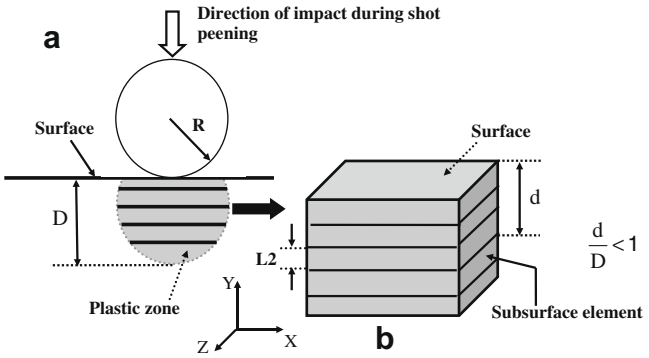

Fig. 4. (a) A schematic showing a metallic ball impacting the specimen surface during shot peening, inducing constrained plastic deformation to a depth D below surface and (b) an equivalent volume element of the plastic zone divided into several subsurface layers ('elements'), each corresponding to a depth d below the surface at which shot peening and fatigue simulations are performed.

1. Consider a homogeneous matrix subsurface element of the specimen at a depth *d* below surface, initially without inclusions, as shown in Fig. 5a. The carburized material properties corresponding to the depth *d* is assigned to the subsurface element.
2. Imposing the boundary conditions shown in Fig. 5, the subsurface element is subjected to uniaxial compression in direction Y to strain levels calculated from the elasto-plastic constitutive relations, in connection with the following step (ε_{yy}^{load} in Fig. 5b). The total strain components (elastic plus plastic) in the *X* and *Z* directions are assumed as zero at each stage of the process, in accordance with overall constraints.
3. The compression is followed by unloading in direction Y (ε_{yy}^{final} in Fig. 5b) to elastic strain levels that match the measured macroscopic residual stress distribution in the material as a function of depth (Fig. 5c).

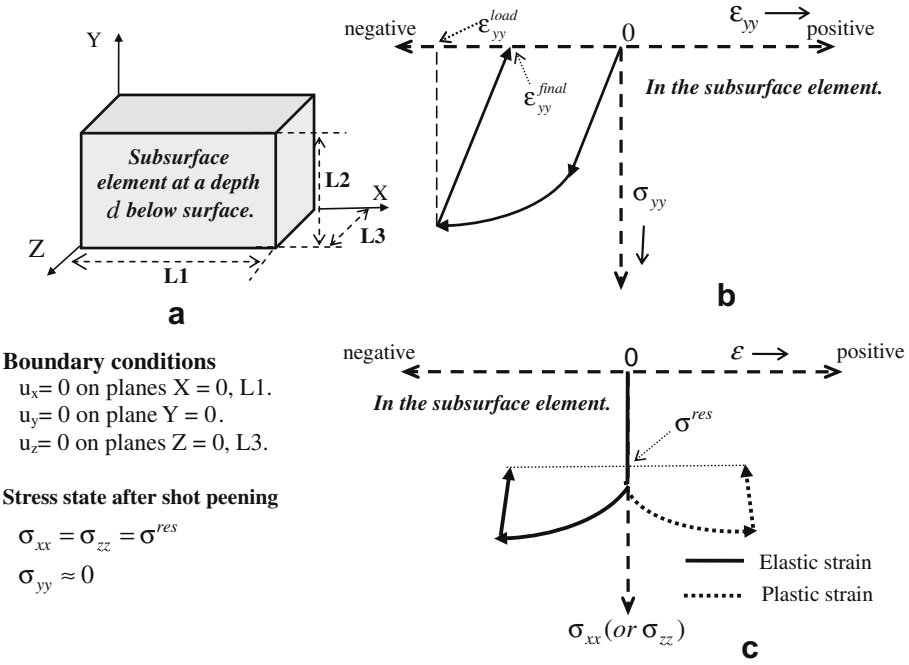

Fig. 5. Methodology to simulate the shot peening process: (a) schematic showing a subsurface element on which the strains are imposed, (b) σ_{yy} vs ε_{yy} response in the subsurface element during shot peening simulation, and (c) variation of elastic and plastic strain in X and Z directions in the subsurface element during shot peening.

4. The resulting strain–time history is then applied as boundary conditions on the same subsurface element with embedded inclusions that are intact, debonded or cracked to assess the local residual stresses and strains in the vicinity of inclusions as initial conditions for subsequent fatigue simulations. This is repeated for each subsurface depth of interest.

When considering the embedded inclusion(s) in Step 4, the dimensions of the subsurface element are chosen to be sufficiently large that the inclusion experiences negligible boundary interaction effects (i.e., boundary conditions obtained from Steps 1–3 are adequate). There is an additional consideration that the gradient of the residual stress state cannot be too large compared to the thickness of the subsurface volume element selected in Step 1; this is dictated by inclusion size. A detailed derivation of the approach outlined in Steps 1–3 above appears in Appendix A. The following direction convention holds for all subsequent 3D calculations:

- Direction of impact (shot peening) –*Y* direction
- Equibiaxial residual stress state –*X* and *Z* directions
- Cyclic loading – bending stress along *Z* direction

It is noted that damage (cracking or debonding) can occur to inclusions during primary forming or shot peening. We therefore pursue the strategy of simulating inclusions that are assumed to be already cracked or debonded at the beginning of the shot peening process as a means of assessing their influence on the local residual stress state and the driving forces for fatigue crack nucleation at the inclusion.

6. Fatigue crack nucleation analysis under cyclic loading

Three-dimensional FE simulations were performed to parametrically explore the relative potency for fatigue crack nucleation at depths ranging from 75 μm to 300 μm below the surface. Idealized shapes of inclusions (ellipsoidal) were employed. Fig. 6 shows a cross-section of a 3D FE mesh with closely spaced inclusions. A fine mesh is employed close to the inclusion(s) for detailed investigation of deformation and stress state in the proximity of the inclusions. All simulations were performed using 4-node 3D tetrahedral elements.

It was assumed that the inclusion sizes are small enough that the gradient of applied stress and residual stress over the scale of an inclusion is negligible. With this assumption, the stress state is imposed at discrete depths within the subsurface inclusion-matrix volume element and the stress and plastic strain components around the inclusion(s) are computed. Fig. 7 shows the

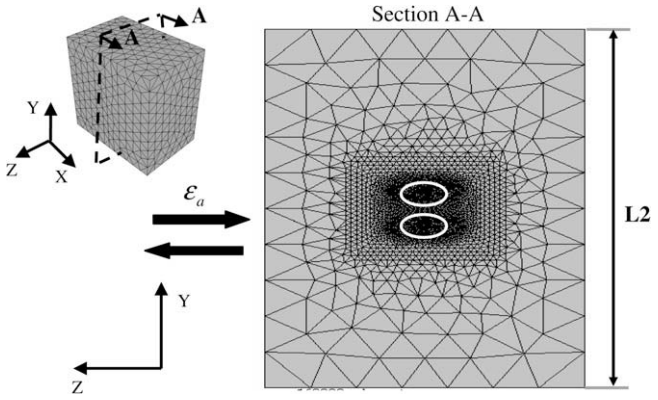

Fig. 6. Cross-section of FE mesh through the center of inclusion with refinement close to the inclusion.

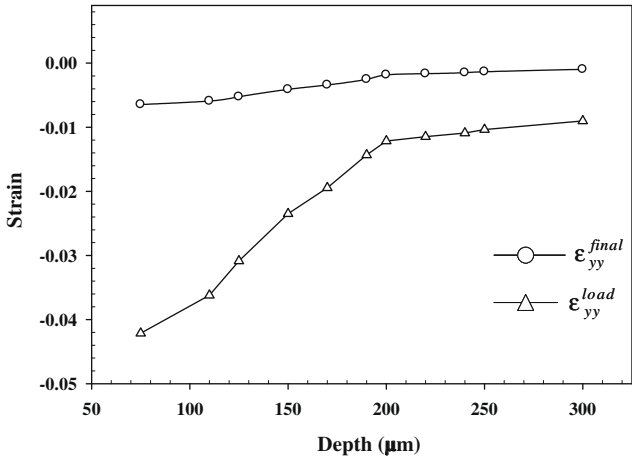

Fig. 7. Variation of the peak compressive strain (ε_{yy}^{load}) and the strain after unloading (ε_{yy}^{final}) along surface normal direction *Y* during shot peening simulation with depth.

variation of peak applied uniaxial compressive strain, $\varepsilon_{yy}^{\text{load}}$, and strain after unloading, $\varepsilon_{yy}^{\text{final}}$, with depth for C61 gear steel during the shot peening simulation. The numerical estimate of strain levels to be imposed to mimic shot peening effect utilizes experimental residual stress value corresponding to the depth of interest as input. For pure matrix without inclusions, the numerical and experimental residual stress values coincide. While simulating the residual stress distribution corresponding to various case depths, we interpolate for the depth where the residual stresses were not measured, with the limited available experimental data. It is noted that when the interval between two neighboring measuring points is smaller, the confidence in the interpolated result is greater. Additionally, between 200 and 300 μm below the surface, the variation in the residual stress magnitude is relatively small, and the interpolation scheme is reasonable. The simulation that imposes residual stress is followed by three cycles of strain-controlled loading with $R_\varepsilon = 0.05$ (applied strain ratio). Fig. 8 shows the variation with depth of the peak applied strain during cyclic bending. The remote applied stress pertains to HCF loading conditions and residual stress relaxation may not be significant; however, the local plasticity in the vicinity of primary inclusions can alter the residual stress state and thereby influence the driving force for fatigue crack nucleation. Driving forces for crack nucleation are calculated during the third load cycle. Two parameters, namely the nonlocal average maximum plastic shear strain range, $\Delta\gamma_{\max}^{p^*}$, and Fatemi–Socie (FS) parameter, $\Delta\Gamma$, are considered as

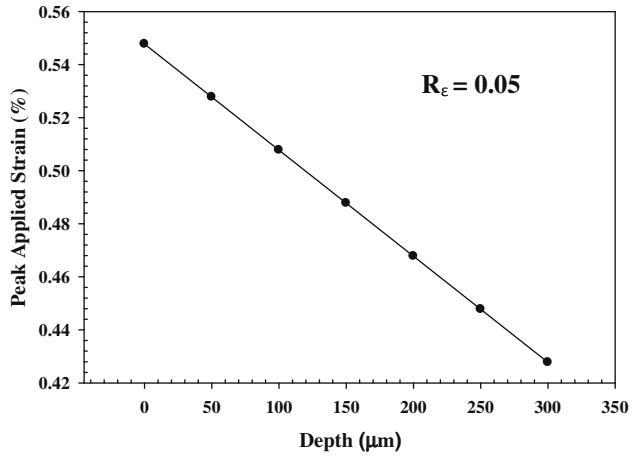

Fig. 8. Peak applied bending strain as a function of depth during cyclic loading.

possible driving force parameters for fatigue crack nucleation at various depths. The latter parameter includes limited consideration of small crack propagation [53]. The FS parameter considers the effect of the maximum normal stress $\sigma_n^{\max}$ perpendicular to the plane of maximum cyclic plastic shear strain, and has proven to be a very effective correlative parameter for multiaxial fatigue [54]. It has been generalized by McDowell [55] and Shenoy et al. [56] to form the basis for microstructure-sensitive small crack growth laws, with the latter study using computational micromechanics to compute the FS parameter within individual grains in a polycrystalline Ni-base superalloy. Good correlations with experiments have been obtained in terms of fatigue lives of different metallic materials using the FS critical plane approach [57–62]. The FS parameter is defined by

$$\Delta\Gamma = \frac{\Delta\gamma_\theta^p}{2}\left(1 + k\frac{\sigma_n^{\max}}{\sigma_{ys}}\right) \tag{7}$$

where, $k = 0.6$ is a material parameter [43].

In local FE analyses, the micronotch root maximum plastic shear strain amplitude is mesh sensitive. Furthermore, fatigue cracks form over some finite region of intense shear, typically on the order of a micron in scale. Moreover, for cracks growing in a notch root field, a transition crack length on the order of 10–20% of the notch root radius is often invoked, below which it is assumed that the local notch root field controls behavior and above which the notch becomes part of the crack. It is therefore necessary to introduce a nonlocal volume averaging procedure over integration points in the mesh to (i) effectively remove mesh dependence and (ii) to accord with the physical process zone for subcritical crack formation processes. Motivated by earlier work [18,38] the maximum plastic shear strain amplitude is averaged over 1 μm^3 (unit cube), which corresponds to about 10% of the volume of an inclusion of minimum size in the present study, and in each simulation is selected as that particular volume of matrix material at the notch root that maximizes the nonlocal plastic shear strain amplitude. We employ this nonlocal volume for all the cases examined in this parametric computational study. Naturally, such a small volume is considered in terms of evaluating the probability to form a crack, and larger domains would be necessary to consider propagation resistance.

At every integration point lying within the nonlocal averaging region, the plastic shear strain γ_θ^p is computed on the plane-θ by projecting onto it the plastic strain tensor ε_{ij}^p at each integration point, i.e.,

$$\frac{\gamma_\theta^p}{2} = n_i\varepsilon_{ij}^p t_j \qquad \theta = 1 \ldots N \tag{8}$$

where n_i and t_j are the unit normal and tangent vectors, respectively, on the plane- θ, and N is the number of discrete planes. The nonlocal average plastic shear strain is then calculated by averaging over the volume V of the nonlocal region, i.e.,

$$\gamma_\theta^{p^*} = \frac{1}{V}\int_V \gamma_\theta^p \mathrm{d}V \tag{9}$$

The nonlocal cyclic plastic shear strain range for every plane is calculated during the third load cycle of the simulation. The nonlocal maximum cyclic plastic shear strain range, is defined by

$$\Delta\gamma_{\max}^{p^*} = \max_\theta(\Delta\gamma_\theta^{p^*}) \tag{10}$$

Once the critical plane and corresponding nonlocal maximum plastic shear strain range are determined, $\Delta\Gamma$ is calculated using Eq. (7) at every integration point on the critical plane and a volume average is performed in the nonlocal region similar to Eq. (9); this effectively results in a nonlocal FS parameter. Alternatively, direct maximization of $\Delta\Gamma$ could be considered instead of first maximizing $\Delta\gamma_{\max}^{p^*}$. A simple local form of the Coffin-Manson law has been used to correlate the number of cycles for nucleation of fatigue cracks with the candidate driving forces [41,63], but of course more complex analyses can be conceived that reflect lower scale details of microstructure and slip irreversibility.

7. Results and Discussion

7.1. Cracked inclusion analyses

Subsurface layers with cracked ellipsoidal inclusions, embedded in the elasto-plastic matrix, were subjected to boundary conditions during shot peening based on the analyses conducted without inclusions, as described earlier. Ellipsoidal inclusions were chosen to facilitate parametric studies; however, inclusion morphology can influence the local stresses and cyclic plastic strain distribution. Investigation of realistic particle shape and distribution will be performed in future. Each layer was then subjected to three cycles of strain-controlled cycling with amplitude appropriate for each depth, and an R ratio of 0.05. Simulations were also performed with intact particles and results showed negligibly small driving force in this study for all case depths below the surface. Similar observations were reported by Gall and co-workers [18] for A356 aluminum alloy. This may be due to the fact that the peak applied bending stress is less than $\leqslant 0.8\sigma_{ys}$ and hence the stress amplitude is well below the elastic limit of C61 gear steel. Also, localization of stresses and plastic strains around intact particles are not as intense as that observed near damaged particles. In addition to the aforementioned observations, it is important to note that fatigue crack nucleation in the high cycle fatigue regime is highly heterogeneous at the grain scale [63]. Investigation of the potency of intact particles to nucleate fatigue cracks while operating close to a fatigue limit associated with nonpropagating cracks demands more detailed scale-dependent, discrete dislocation plasticity simulations; J_2 plasticity assumption may not be sufficient to reflect such failure scenarios. Accordingly, this ideal case study focuses on cracks nucleating from damaged particles (cracked and partially debonded inclusions) for which plastic strain localization in the matrix is of sufficient magnitude to merit treatment with simple J_2 plasticity to facilitate parametric comparisons.

Fig. 9 illustrates the three-dimensional boundary conditions and orientation of a cracked particle with respect to the direction of applied bending stress and the surface. It was assumed that inclusions tend to crack when the major axis of the ellipsoidal particle is oriented parallel to the applied stress direction. Table 2 summarizes the list of cases considered while analyzing the effect of cracked particles on fatigue crack nucleation in the matrix at various subsurface depths. In Tables 2 and 3, 2a and 2b represent the major and minor axis dimensions of the ellipsoidal inclusion, respectively, 2c and 2d represent those of the neighboring inclusion, and L is the longitudinal end-to-end spacing between the inclusions, chosen to be 1 μm in this limited parametric study. For convenience, all cases and results presented in the subsequent sections will be addressed with the 'case pointer' listed in Table 2. For example, Fig. 10a shows the equivalent plastic strain contour plot around the cracked inclusions located at 250 μm below surface, at the end of the third loading cycle for case R1. The study cases listed in Tables 1 and 2 were chosen in order to examine the factors that affect the severity of plastic strain localization at non-metallic primary inclusions which include inclusion spacing, size, and orientation. The aforementioned factors are important in HCF [63]. A frictionless surface-to-surface contact is used to model all debonded interfaces in this study.

Plastic strain intensification is observed to occur in the matrix near the intersection of the cracked particle with the matrix. The

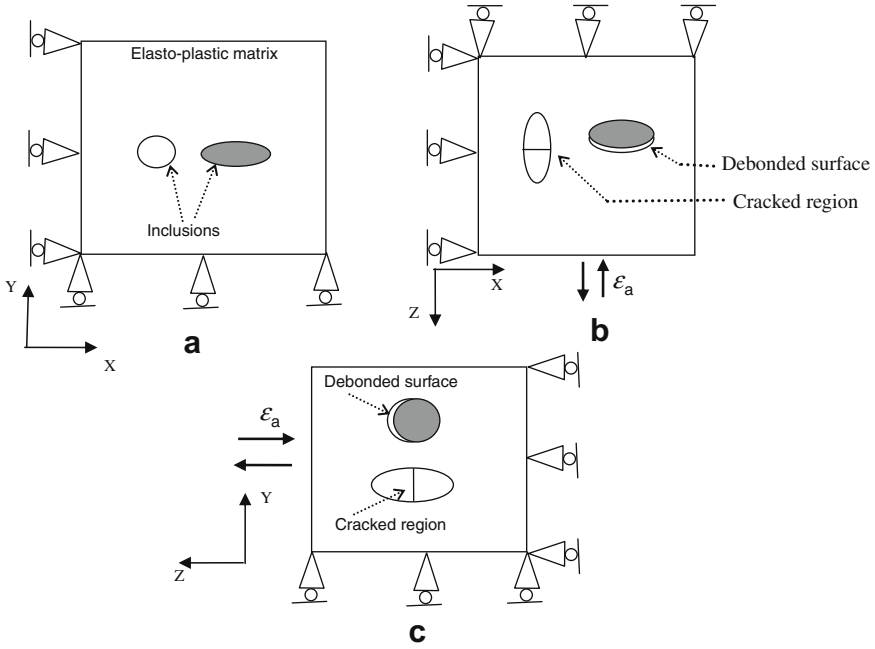

Fig. 9. Cross-sectional views of the 3D section with embedded inclusions, showing the debonded and cracked surfaces, boundary conditions for bending, and cyclic loading direction. Views on (a) *XY*, (b) *XZ*, and (c) *YZ* cutting planes through the center of the inclusion.

Table 2
List of cases analyzed in the study of cracked inclusions.

Case pointer	No of inclusions	Shape of inclusion	2a (μm)	2b (μm)	2c (μm)	2d (μm)	L (μm)
P1	1	Ellipsoidal	5	2	–	–	–
Q1	2	Ellipsoidal	5	2	5	2	1
R1	2	Ellipsoidal	5	2	10	4	1

Table 3
List of cases analyzed in the study of partially debonded inclusions.

Case Pointer	No. of Inclusions	Shape of inclusion	2a (μm)	2b (μm)	2c (μm)	2d (μm)	*L* (μm)	ϕ_1	ϕ_2
A1	1	Ellipsoidal	5	2	–	–	–	0°	–
B1	2	Ellipsoidal	5	2	5	2	1	0°	0°
C1	2	Ellipsoidal	5	2	5	2	1	90°	90°
D1	2	Ellipsoidal	5	2	10	4	1	0°	0°
E1	2	Ellipsoidal	5	2	10	4	1	90°	90°

ϕ_1 and ϕ_2 represent the orientation of inclusion 1 and inclusion 2, respectively)

severity of stresses and plastic strain localization was observed to depend on the size of the inclusion and inclusion spacing. The highest values of stresses and plastic strains were observed in case R1 as compared to cases P1 and Q1 in the vicinity of cracked particle. Stress intensification arising due to interaction of inclusions could magnify the crack driving force and thereby reduce the fatigue crack nucleation and early growth life relative to the case of a single inclusion. An example of a detailed investigation of the effect of particle shape, alignment, spacing and configuration on local stress distribution under cyclic loading can be found elsewhere [64].

Fig. 11 shows the variation of the nonlocal maximum plastic shear strain amplitude, $\Delta\gamma^{p^*}_{\max}/2$, and nonlocal FS parameter, $\Delta\Gamma$, with depth for case P1. Interestingly, the maximum value of these parameters corresponds to a depth of about 250 μm below the surface, which falls within the range of depths observed in experiments for C61 gear steels. Note that this depth is still within the regime of initial compressive residual stress following shot peening. The driving forces are negligibly small at depths between 75 and 150 μm even though the applied strain amplitude is higher close to the surface. Shot peening suppresses the fatigue crack nucleation at the surface and shifts the crack nucleation site to subsurface depths. The critical depth depends on residual stress distribution, applied stress, and property gradients. Presence of other inhomogeneities such as pores and soft inclusions (sulfide particles) could alter the favorable site for crack nucleation depending on the intensity of localization around such inclusions.

The nonlocal maximum plastic shear strain amplitude and FS parameter were also calculated for cases with two cracked inclusions closely spaced (case Q1and R1); results are shown in Figs. 12 and 13, respectively. The trends are similar to that of the single cracked inclusion (case P1) but the values are an order of magnitude higher due to size and interaction of inclusions. Increase of the fatigue crack nucleation driving force with increase in inclusion size (case R1 compared to case Q1) supports the observation of Toyoda and co-workers [21] relating the inclusion size to threshold fatigue strength. The sensitivity of potency of fatigue crack nucleation to the size and number of particles (clustering) is most

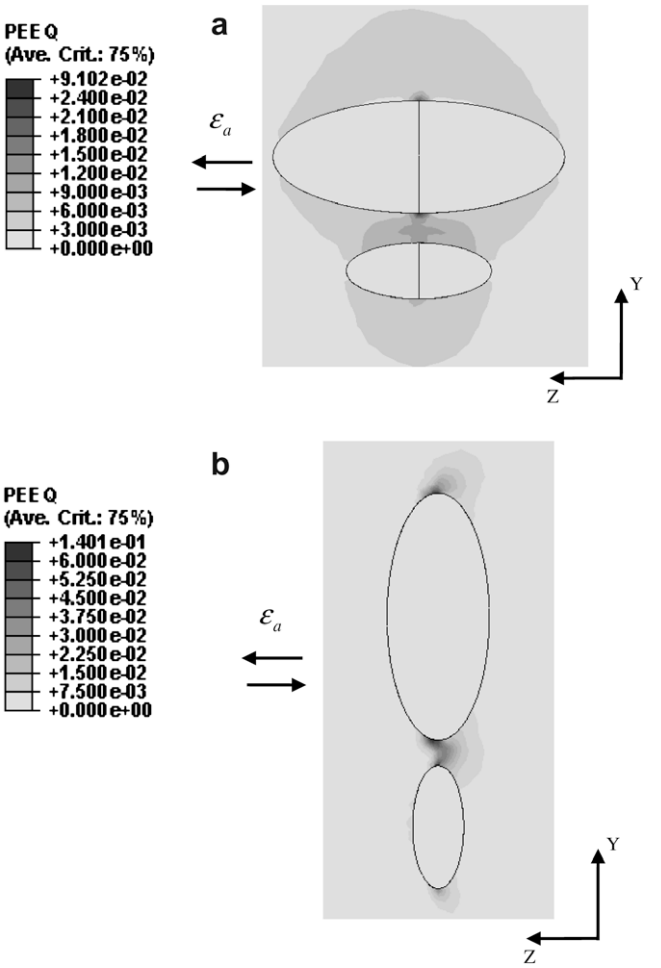

Fig. 10. Contour plot of the equivalent plastic strain at the end of third loading cycle at a depth of 250 μm below surface: (a) case R1 and (b) case E1.

pronounced at lower stress levels than at stress levels above macroscopic yielding [41]. Several other factors affect the HCF crack nucleation life, including inclusion shape and orientation [17,40,64]. However, detailed investigation of all the factors influencing subsurface fatigue crack nucleation in shot peened C61 steel is beyond the scope of the present parametric study.

7.2. Partially debonded inclusion analyses

Three-dimensional FE analyses were performed involving partially debonded inclusions (ellipsoidal) embedded in an elasto-plastic matrix. McDowell et al. [17] showed for A356-T6 Al alloy that partially debonded inclusions offer the most conservative (i.e., severe) scenario for assessment of fatigue potency. Fig. 14 describes the convention followed to represent ellipsoidal inclusion orientation in XY plane denoted by angle φ. In all cases, the ellipsoidal inclusions were aligned such that the major axis of the inclusion was perpendicular to the direction of applied bending stress. Fig. 9 shows cross-sectional views of the 3D domain, elaborating on the boundary conditions, loading direction, and debonded surface of the inclusion considered in the parametric study.

Each subsurface volume element was subjected to similar loading conditions as described in cracked inclusion analyses. Table 3 summarizes the different cases of a partially debonded inclusion analyzed in the parametric study. All the cases presented in the following plots and discussion will be addressed with the 'case pointer' listed in Table 3. For example, Fig. 10b shows the equivalent plastic strain contour plot for case E1 at the end of the third loading cycle. Intensified plastic strain at the intersection of the debonded and bonded surfaces of the matrix can be observed in the contour plot. The intensification is due to the crack-like defect present at the tip of the debond seam coupled with the constraint and contact of embedded inclusions. It was mentioned by Gall et al. [18] that high stresses around cracked inclusions can facilitate debonding at the particle matrix interface. It was also shown that once a cracked particle begins to debond, the local plastic strains are intensified in the matrix with the same order of magnitude as a crack-free but partially debonded inclusion. Similar to cracked inclusion analyses, the severity of stress and plastic strain localization was influenced by particle size and spacing. The magnitudes of plastic strains and stresses in the matrix encompassing the partially debonded alumina inclusion were highest in cases D1 and E1 compared to all other cases listed in Table 3.

Fig. 15 shows the variation of nonlocal maximum plastic shear strain amplitude and nonlocal FS parameter with depth for case A1. Similar to the results obtained in the cracked inclusion analyses, the critical depth for fatigue crack nucleation trends towards 250 μm. The debonded inclusion is observed to facilitate higher plastic strains under monotonic loading, which in turn leads to higher local stress states. Consequently, reversed yielding occurs more readily near the debonded inclusion. Consistent results were obtained for all the cases listed in Table 3 (see Figs. 16–19) where

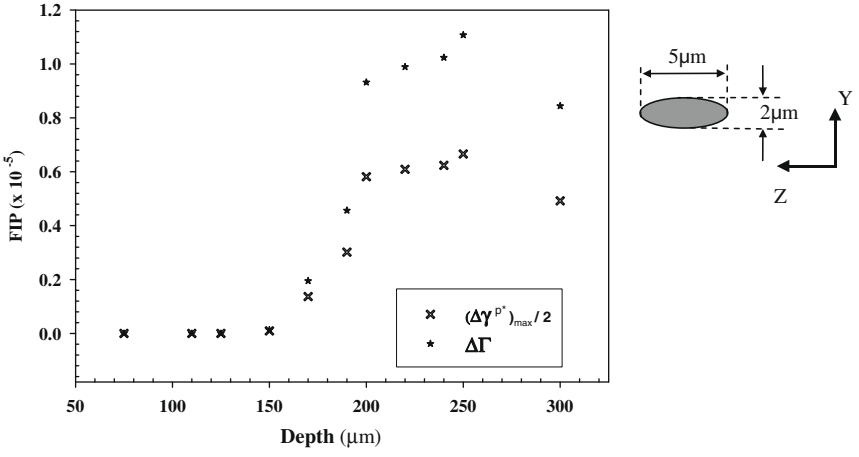

Fig. 11. Variation of nonlocal maximum cyclic plastic shear strain amplitude and FS parameter with depth for case P1.

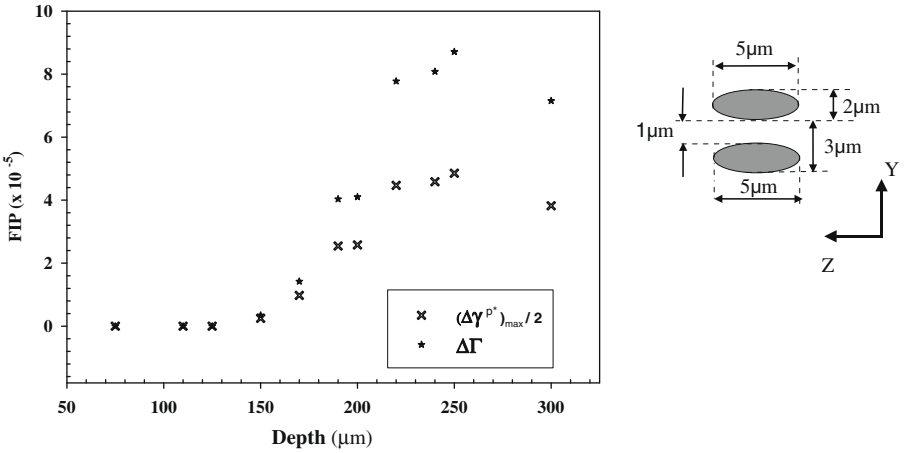

Fig. 12. Variation of nonlocal maximum cyclic plastic shear strain amplitude and FS parameter with depth for case Q1.

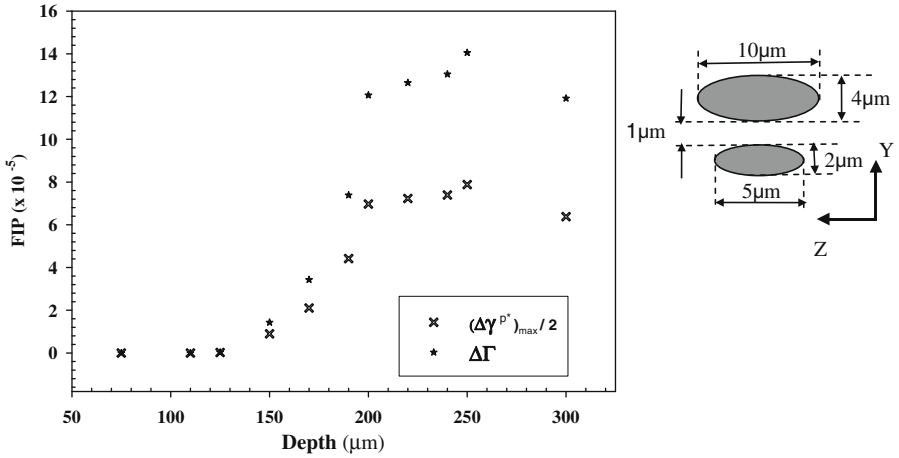

Fig. 13. Variation of nonlocal maximum cyclic plastic shear strain amplitude and FS parameter with depth for case R1.

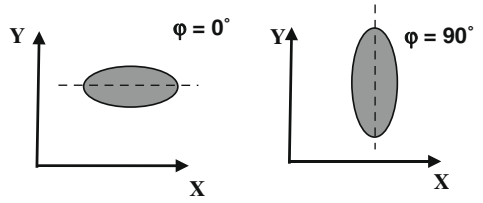

Fig. 14. Convention followed to represent the orientation of inclusion. Angle φ is measured with respect to *X* axis (axis of applied bending strain along *Z* direction). Direction *Y* is normal to the surface.

the predicted critical depth for subsurface fatigue crack nucleation was in accordance with experimental observations. Size and spacing of partially debonded inclusions are observed to play a significant role in fatigue crack nucleation potency at subsurface depths. Case E1 is observed to be most detrimental under cyclic loading among all cases analyzed in this parametric study. This is due to the presence of a large partially debonded inclusion coupled with intensification arising due to interaction with neighboring inclusion. The variations arising due to spatial alignment of inclusions in a cluster (comparing case D1 and case E1) will be addressed later. The predictions and observations reported in this parametric study emphasize the importance of inclusion-matrix interface character on fatigue crack nucleation potency. Comparing the single cracked particle results (case P1) in Fig. 11 and single partially debonded inclusion results (case A1) in Fig. 15 for which the inclusion size was equal, the driving force for fatigue crack nucleation is relatively higher in presence of partially debonded inclusions. Similar observations can be made by comparing different cases of partially debonded and cracked inclusions with equal size and spacing; it is evident that cracked inclusions do not localize plastic strains and stresses in the matrix as severely as partially debonded inclusions.

The use of ellipsoidal inclusions in this parametric study facilitates assessment of the effect of inclusion alignment in a cluster with respect to loading direction on fatigue crack nucleation. Although partially debonded inclusions were aligned such that the major axis of the ellipsoid was perpendicular to loading direction, some disparity in the driving force for fatigue crack nucleation arises by varying the relative alignment of inclusions in the *XY* plane. The differences were significant between case D1 (Fig. 18) and case E1 (Fig. 19). The driving force parameters are relatively higher at subsurface depths for case E1. Since the plastic strain localization is most severe at the inclusion notch root in ellipsoidal particles, the magnitudes of these parameters are expected to be relatively higher when the inclusions are aligned such that the major axis of individual inclusions coincides (as in case E1). Comparing cases B1 and C1 in Figs. 16 and 17, respectively, the difference in the magnitudes of FIPs are relatively small. This observation suggests that the effect of

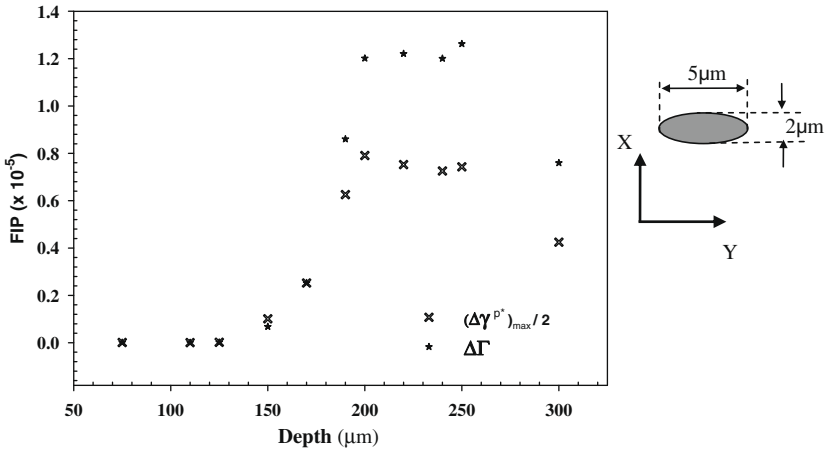

Fig. 15. Variation of nonlocal maximum cyclic plastic shear strain amplitude and FS parameter with depth for case A1.

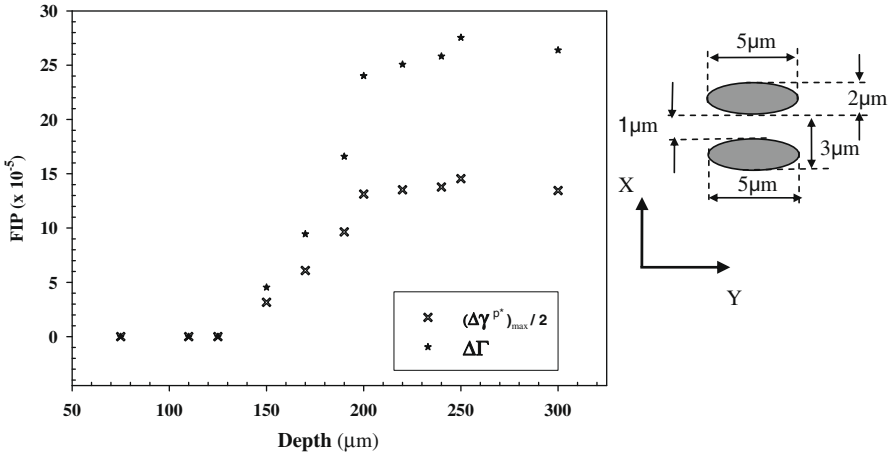

Fig. 16. Variation of nonlocal maximum cyclic plastic shear strain amplitude and FS parameter with depth for case B1.

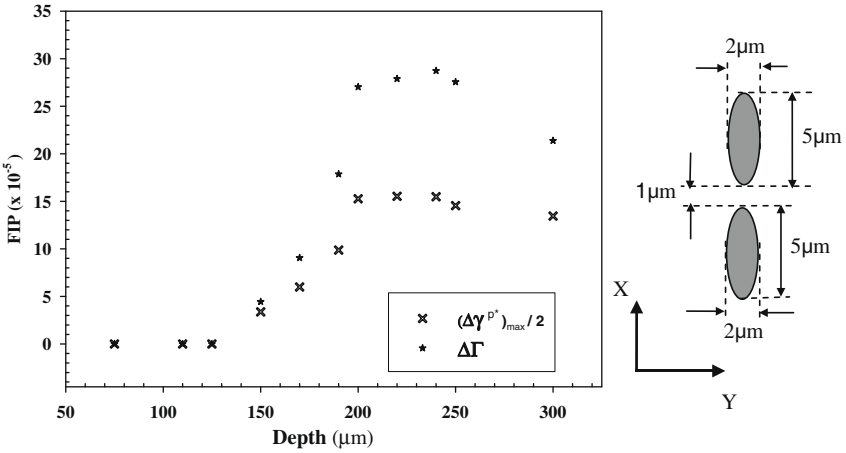

Fig. 17. Variation of nonlocal maximum cyclic plastic shear strain amplitude and FS parameter with depth for case C1.

relative spatial alignment of inclusions in a cluster on fatigue crack nucleation is more pronounced for large inclusions ($\geqslant$10 μm) and can be regarded as a second-order effect. The disparity in fatigue response arising due to variations in spatial arrangement of inclusions in a cluster can be a major contributor to the scatter in HCF lives observed in experiments. In addition to the intensification of the driving force for nucleation, the size of the embryo for long crack growth is on the order of the cluster size, which can be substantially larger than the size of individual primary inclusions (see Fig. 2). Study of subcritical crack formation and growth within inclusion clusters of more complex character is a topic of ongoing work.

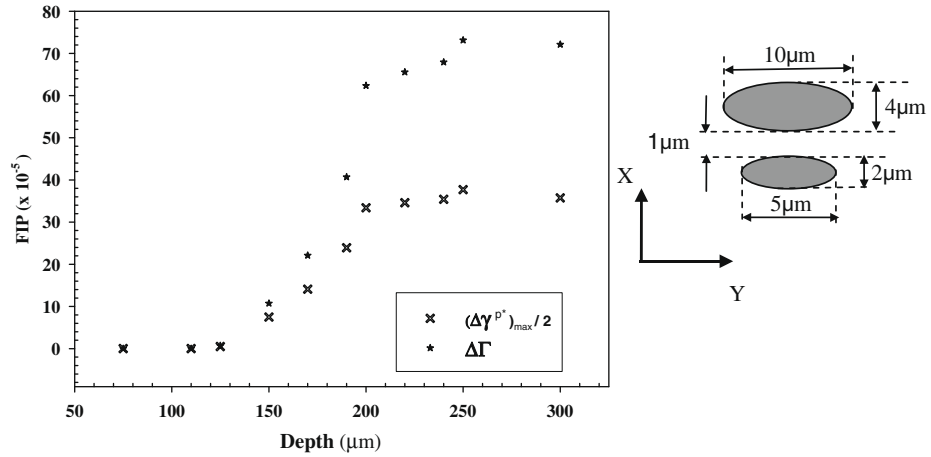

Fig. 18. Variation of nonlocal maximum cyclic plastic shear strain amplitude and FS parameter with depth for case D1.

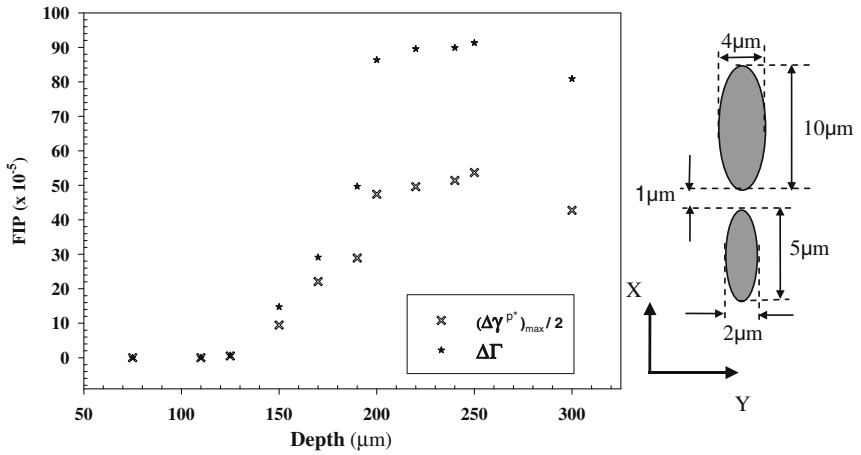

Fig. 19. Variation of nonlocal maximum cyclic plastic shear strain amplitude and FS parameter with depth for case E1.

It is evident from cases D1, E1 and R1 that the presence of large inclusions has more detrimental effect under cyclic loading. This is widely acknowledged from the perspective of initial flaw size, treating the inclusion as an initial crack starter for application of fracture mechanics. In this work, we undertake a different approach that focuses more on the details of inclusion size, spacing, interface character and residual stresses on HCF response.

8. Summary

Finite element modeling is used to parametrically study the effects of process history and and non-metallic inclusions on the high cycle fatigue of a martensitic gear steel. Significant contributions and findings of this work are as follows.

(1) A simplified algorithm is presented to simulate the residual stress distribution induced by shot peening prior to applying a fatigue loading history, including effects of cracked and debonded subsurface inclusions on local residual stresses.
(2) An integrated three-dimensional methodology is developed to analyze potency of fatigue crack nucleation at subsurface primary inclusions in carburized and shot peened gear steels. The methodology was applied to predict the favorable depth for fatigue crack nucleation in C61 alloy gear steel, with predicted depths in accordance with experimental observations [1]. Fatigue crack nucleation occurs in a depth range where the initial residual stresses are compressive (not tensile) following shot peening.
(3) Under the given external loading, material model, and the selected fatigue crack nucleation driving force parameter, intact inclusions were observed to show negligible driving force for crack nucleation in the HCF regime. Pre-existing damage from primary forming or from shot peening processes, such as partially debonded inclusion–matrix interfaces, promoted fatigue crack nucleation.
(4) The driving force for subsurface fatigue crack nucleation depends on size and clustering of inclusions. Relative alignment of inclusions in a cluster was observed to influence the driving force for fatigue crack nucleation in presence of sufficiently large inclusions ($\geqslant$ 10 μm). Presence of large inclusions in addition to clusters has detrimental effects under cyclic loading.

Future work will address mechanisms specific to the martensitic microstructure in the matrix with regard to crack formation and early growth to refine the framework presented here. In addition, relaxation of residual stress during fatigue cycling can be very important even in the HCF regime [65–67], and must be studied using more refined material models such as polycrystal plasticity. The framework developed here can be readily extended to consider this effect.

Acknowledgments

The authors are grateful for the support of the ONR/DARPA D3D tools consortia (J. Christodoulou, monitor), under contract # N00014-05-C-0241. The authors also thank Mahesh Shenoy for the helpful discussions during the course of this work.

Appendix A

The stress state at any subsurface depth after shot peening is given by

$$\begin{aligned}&\sigma_{xx}=\sigma_{zz}=\sigma^{res}\\&\sigma_{yy}=0\\&\tau_{xy}=\tau_{xz}=\tau_{yz}=0\\&\alpha_{xy}=\alpha_{xz}=\alpha_{yz}=0\end{aligned}\tag{A.1}$$

During plastic deformation (shot peening), the following quantities and their differential increments always satisfy

$$\begin{aligned}&\varepsilon^p_{xy}=\varepsilon^p_{xz}=\varepsilon^p_{yz}=0\quad \mathrm{d}\varepsilon^p_{xy}=\mathrm{d}\varepsilon^p_{xz}=\mathrm{d}\varepsilon^p_{yz}=0\\&\varepsilon^p_{xx}+\varepsilon^p_{yy}+\varepsilon^p_{zz}=0 \text{ and } \mathrm{d}\varepsilon^p_{xx}+\mathrm{d}\varepsilon^p_{yy}+\mathrm{d}\varepsilon^p_{zz}=0 \text{ (incompressibility)}\\&\varepsilon^p_{xx}=\varepsilon^p_{zz}=-\frac{1}{2}\varepsilon^p_{yy}\quad \mathrm{d}\varepsilon^p_{xx}=\mathrm{d}\varepsilon^p_{zz}=-\frac{1}{2}\mathrm{d}\varepsilon^p_{yy}\end{aligned}\tag{A.2}$$

During the shot peening process the shear strain components are zero in the XYZ principal coordinate frame, i.e.,

$$\varepsilon_{xy}=\varepsilon_{yz}=\varepsilon_{zx}=0\tag{A.3}$$

Expanding the yield function in Eq. (1) gives

$$\begin{aligned}F=&\left[2(\sigma_{xx}-\alpha_{xx})-(\sigma_{yy}-\alpha_{yy})-(\sigma_{zz}-\alpha_{zz})\right]^2\\&+\left[2(\sigma_{zz}-\alpha_{zz})-(\sigma_{xx}-\alpha_{xx})-(\sigma_{yy}-\alpha_{yy})\right]^2\\&+\left[2(\sigma_{yy}-\alpha_{yy})-(\sigma_{xx}-\alpha_{xx})-(\sigma_{zz}-\alpha_{zz})\right]^2-6\sigma^2_{ys}\\=&0\end{aligned}\tag{A.4}$$

Due to equi-biaxial deformation, the following relationships hold during the entire process of shot peening:

$$\begin{aligned}&\sigma_{xx}-\alpha_{xx}=\sigma_{zz}-\alpha_{zz}\\&S_{xx}-\alpha'_{xx}=S_{zz}-\alpha'_{zz}\\&\varepsilon^p_{xx}=\varepsilon^p_{zz},\quad \dot{\varepsilon}^p_{xx}=\dot{\varepsilon}^p_{zz}\end{aligned}\tag{A.5}$$

Inserting Eq. (A.5) into Eq. (A.4) the yield function reduces to

$$\begin{aligned}&F=\left[(\sigma_{xx}-\alpha_{xx})-(\sigma_{yy}-\alpha_{yy})\right]^2-\sigma^2_{ys}=0 \text{ or}\\&\left|(\sigma_{xx}-\alpha_{xx})-(\sigma_{yy}-\alpha_{yy})\right|=\sigma_{ys}\end{aligned}\tag{A.6}$$

Using the relation in Eq. (A.2) the increment of equivalent plastic strain is given by,

$$d\bar{\varepsilon}^p=|d\varepsilon^p_{yy}|=2|d\varepsilon^p_{xx}|\tag{A.7}$$

Using the three-dimensional Hooke's law, the elastic and plastic strains at the end of shot peening process can be obtained by applying the boundary conditions shown in Fig. 5, i.e.,

$$\begin{aligned}&\varepsilon^{e,final}_{xx}=\frac{\sigma^{res}}{E}(1-\nu)=-\varepsilon^{p,final}_{xx}\\&\varepsilon^{e,final}_{zz}=\frac{\sigma^{res}}{E}(1-\nu)=-\varepsilon^{p,final}_{zz}\\&\varepsilon^{e,final}_{yy}=\frac{-\nu}{E}(2\sigma^{res})\end{aligned}\tag{A.8}$$

Here, the superscript '*final*' corresponds to final strain state at the end of shot peening. Coupling Eqs. (A.2), (A.7), and (A.8), the final strain component along direction Y after unloading can be obtained as

$$\varepsilon^{final}_{yy}=\frac{-\nu}{E}(2\sigma^{res})+2\varepsilon^{e,final}_{xx}\tag{A.9}$$

In order to obtain the peak uniaxial compressive strain to be imposed along direction Y (ε^{load}_{yy}) to induce the target residual stress level, the above equations coupled with the nonlinear kinematic hardening relation described in Eq. (5) are solved numerically. We employ the method of successive substitution along with an interval-halving scheme to iteratively solve the set of equations. The return mapping scheme to solve the elasto-plastic relations (Eqs (1)–(6)) is implemented along the lines proposed by Kobayashi and Ohno [68].

References

[1] Tiemens BL. Performance optimization and computational design of ultra-high strength gear steels. Department of materials science and engineering. PhD thesis, Evanston (IL): Northwestern University, 2006.
[2] Tiemens BL, Sachdev AK, Olson GB. Performance of computationally designed ultra-hard steel for transmission gear applications. Collaborate report CL -04/41/MPL, GM Research and Development Center, August 2004.
[3] Ceschini L, Minak G. Fatigue behaviour of low temperature carburised AISI 316L austenitic stainless steel. Surf Coat Technol 2008;202(9):1778–84.
[4] Tokaji K, Akita M. Effect of carburizing on notch fatigue behaviour in AISI 316 austenitic stainless steel. Surf Coat Technol 2006;200(20-21):6073–8.
[5] Farfan S, Rubio-Gonzalez C, Cervantes-Hernandez T, Mesmacque G. High cycle fatigue, low cycle fatigue and failure modes of a carburized steel. Int J Fatigue 2004;26(6):673–8.
[6] Kawagoishi N, Nagano T, Moriyama M. Effect of shot peening on fatigue strength of maraging steel. Sixth international conference on computer methods and experimental measurements for surface treatment effects,Crete, Greece 2003; 7:99–108.
[7] Iwata N, Tomota Y, Katahira K, Suzuki H. Effect of shot peening on fatigue fracture for an as quenched martensitic steel. Mater Sci Technol 2002;18(6):629–32.
[8] Brown J. Shot peening increases gear life. Power Transmission Des 1996;38(5):61–4.
[9] Benedetti M, Fontanari V, Hohn BR, Oster P, Tobie T. Influence of shot peening on bending tooth fatigue limit of case hardened gears. Int J Fatigue 2002;24(11):1127–36.
[10] Almen JO. Fatigue weakness of surfaces. Prod Eng 1950;21(11):117–40.
[11] Sieber R. Bending fatigue performance of carburized gear steels. SAE International congress and exposition detroit, MI. Warrendale (PA), SAE; 1992: p. 1–18.
[12] Kunio T, Shimizu M, Yamada K, Sakura K, Yamamoto T. Early stage of fatigue crack growth in martensitic steel. Int J Fracture 1981;17(2):111–9.
[13] Murakami Y, Endo T. Effects of small defects on fatigue strength of metals. Int J Fatigue 1980;2(1):23–30.
[14] Murakami Y, Endo M. Quantitative evaluation of fatigue strength of metals containing various small defects or cracks. Eng Fracture Mech 1983;17(1):1–15.
[15] Umezawa O, Nagai K. Deformation structure and subsurface fatigue crack generation in austenitic steels at low temperature. Metall Mater Trans A (Phys Metall Mater Sci) 1998;29A(3):809–22.
[16] Wang QY, Bathias C, Kawagoishi N, Chen Q. Effect of inclusion on subsurface crack initiation and gigacycle fatigue strength. Int J Fatigue 2002;24(12):1269–74.
[17] McDowell DL, Gall K, Horstemeyer MF, Fan J. Microstructure-based fatigue modeling of cast A356-T6 alloy. Eng Fract Mech 2003;70(1):49–80.
[18] Gall K, Horstemeyer MF, Degner BW, McDowell DL, Fan J. On the driving force for fatigue crack formation from inclusion and voids in a cast A356 aluminum alloy. Int J Fracture 2001;108(3):207–33.
[19] Torres MAS, Voorwald HJC. An evaluation of shot peening, residual stress and stress relaxation on the fatigue life of AISI 4340 steel. Int J Fatigue 2002;24(8):877–86.
[20] Shaw BA, Aylott C, O'Hara P, Brimble K. In: Hyannis MA, editor. The role of residual stress on the fatigue strength of high performance gearing, vol. 25. United States: Elsevier; 2003. p. 1279–83.
[21] Toyoda T, Matsui T, Murakami Y. A study of inclusions causing fatigue cracks in steels for carburized and shot peened gears. JSAE Review 1990;11:50–4.
[22] Nishijima S, Kanazawa K. Stepwise S-N curve and fish-eye failure in gigacycle fatigue. Fatigue Fracture Eng Mater Struct 1999;22(7):601–7.
[23] Shiozawa K, Lu L. Very high-cycle fatigue behaviour of shot-peened high-carbon-chromium bearing steel. Fatigue Fracture Eng Mater Struct 2002;25(8-9):813–22.

[24] Kim C, Diesburg DE, Eldis GT. Effect of residual stress on fatigue behavior of carburized steels- an analytical model. In: ASTM STP 776, Residual stress effect in fatigue; 1982; p. 224-234.
[25] Sharma VK, Walter GH, Breen DH. Factors influencing fracture toughness of high carbon martensitic steels. Gear Technol 1989:7–18.
[26] Lin H, Fett GA, Binoniemi RR. Bending fatigue life analysis of carburized components using strain life and fracture mechanics approaches. J Mater Manuf 2004;112:154–64.
[27] MackAldener M, Olsson M. Tooth interior fatigue fracture – computational and material aspects. Int J Fatigue 2001;23(4):329–40.
[28] McDiarmid DL. General criterion for high cycle multiaxial fatigue failure. Fatigue Fracture Eng Mater Struct 1991;14(4):429–53.
[29] Borbely A, Mughrabi H, Eisenmeier G, Hoppel HW. A finite element modelling study of strain localization in the vicinity of near-surface cavities as a cause of subsurface fatigue crack initiation. Int J Fracture 2002;115(3):227–32.
[30] Ogawa K, Asano T. Theoretical prediction of residual stress produced by shot peening and experimental verification for carburized steel. Mater Sci Res Int 2000;6(1):55–62.
[31] Inoue K, Kato M. Crack growth resistance due to shot peening in carburized gears. J Propul Power 1995;11(5):973–9.
[32] Blarasin A, Guagliano M, Vergani L. Fatigue crack growth prediction in specimens similar to spur gear teeth. Fatigue Fracture Eng Mater Struct 1997;20(8):1171–82.
[33] Chaboche JL, Jung O. Application of a kinematic hardening viscoplasticity model with thresholds to the residual stress relaxation. Int J Plasticity 1997;13(10):785–807.
[34] Li JK, Yao M, Wang D. Mechanical approach to the residual stress field induced by shot peening. Mater Sci Eng A (Struct Mater: Properties, Microstruct Process) 1991;A147(2):167–73.
[35] Meguid SA, Shagal G, Stranart JC, Liew KM, Ong LS. Relaxation of peening residual stresses due to cyclic thermo-mechanical overload. J Eng Mater Technol, Trans ASME 2005;127(2):170–8.
[36] Fathallah R, Laamouri A, Sidhom H, Braham C. High cycle fatigue behavior prediction of shot-peened parts. Int J Fatigue 2004;26(10):1053–67.
[37] Yanhuai L, Jian L, Kewei X. Calculation of relaxation of residual stress and change of yield strength in shot peened layer. Mater Sci Forum 2005;490–491:396–403.
[38] Shenoy MM, Kumar RS, McDowell DL. Modeling effects of nonmetallic inclusions on LCF in DS nickel-base superalloys. Int J Fatigue 2005;27(2):113–27.
[39] Melander A. Finite element study of short cracks with different inclusion types under rolling contact fatigue load. Int J Fatigue 1997;19(1):13–24.
[40] Gall K, Yang N, Horstemeyer M, McDowell DL, Jinghong F. The debonding and fracture of Si particles during the fatigue of a cast Al–Si alloy. Metall Mater Trans A (Phys Metall Mater Sci) 1999;30A(12):3079–88.
[41] Fan J, McDowell DL, Horstemeyer MF, Gall K. Cyclic plasticity at pores and inclusions in cast Al-Si alloys. Eng Fract Mech 2003;70(10):1281–302.
[42] Kuehmann CJ, Olson GB. Advanced gear steels by computer-aided design. Adv Mater Process 1998;153:40–3.
[43] Fatemi A, Socie DF. A critical plane approach to multiaxial fatigue damage including out-of-phase loading. Fatigue Fracture Eng Mater Struct 1988;11(3):149–65.
[44] ABAQUS (Ver 6.5).Hibbitt, Karlsson, and Sorensen Inc., Providence, RI; 2005.
[45] ASTM E92-82 standard test method for Vickers hardness of metallic materials; 2003.
[46] Qian Y, Almer J, Lienert U, Tiemens BL, Olson GB. Nondestructive residual stress distribution measurements in nanostructured ultrahigh-strength gear steels. In: 5th International conference on synchrotron radiation in materials science, Chicago; 2006.
[47] Donzella G, Pola A, Solazzi L, Marconi GP. Effect of shot peening on carburized surfaces. Int J Mater Prod Technol 2000;15(1-2):117–30.
[48] Pedersen R, Rice SL. "Case crushing" of carburized and hardened gears. New York (NY): Society of Automotive Engineers (SAE); 1960.
[49] Boller C, Seeger T. Materials data for cyclic loading, part b: low alloy steels. New York: Elsevier; 1987.
[50] ABAQUS/Standard User's Manual (Ver. 6.5). Providence, (RI): HKS Inc., 2005.
[51] Xiao H, Chen Q, Shao E, Wu D, Chen Z, Wang Z. The effect of shot peening on rolling contact fatigue behaviour and its crack initiation and propagation in carburized steel. Wear 1991;151(1):77–86.
[52] Kobayashi M, Matsui T, Murakami Y. Mechanism of creation of compressive residual stress by shot peening. Int J Fatigue 1998;20(5):351–7.
[53] McDowell DL, Berard JY. A ΔJ based approach to biaxial fatigue. Fatigue Fracture Eng Mater Struct 1992;15(8):719–41.
[54] McDowell DL. Multiaxial Fatigue Strength. ASM Handbook; 1996;p. 263–273.
[55] McDowell DL. Multiaxial small fatigue crack growth in metals. Int J Fatigue 1997;19:127–35.
[56] Shenoy M, Zhang J, McDowell DL. Estimating fatigue sensitivity to polycrystalline Ni-base superalloy microstructures using a computational approach. Fatigue Fracture Eng Mater Struct 2007;30(10):889–904.
[57] Jiang Y, Hertel O, Vormwald M. An experimental evaluation of three critical plane multiaxial fatigue criteria. Int J Fatigue 2007;29(8):1490–502.
[58] Kim KS, Park JC. Shear strain based multiaxial fatigue parameters applied to variable amplitude loading. Int J Fatigue 1999;21(5):475–83.
[59] Findley KO, Saxena A. Low cycle fatigue in Rene 88DT at 650 C: crack nucleation mechanisms and modeling. Metall Mater Trans A (Phys Metall Mater Sci) 2006;37A(5):1469–75.
[60] Chen X, Gao Q, Sun XF. Damage analysis of low-cycle fatigue under non-proportional loading. Int J Fatigue 1994;16(3):221–5.
[61] Kwon JD, Park JC. Multiaxial fatigue life prediction of duplex stainless steels with thermal aging at 430 °C under axial-torsional load. Key Eng Mater 2004;270-273:1183–8.
[62] Reis L, De Freitas M. Analytical and experimental studies on fatigue crack path under complex multi-axial loading. Fatigue Fracture Eng Mater Struct 2006;29(4):281–9.
[63] McDowell DL. Simulation-based strategies for microstructure-sensitive fatigue modeling. Mater Sci Eng A 2007;468-470:4–14.
[64] Gall K, Horstemeyer M, McDowell DL, Fan J. Finite element analysis of the stress distributions near damaged Si particle clusters in cast Al–Si alloys. Mech Mater 2000;32(5):277–301.
[65] Teodosio JR, Fonseca MC, Pedrosa PD. Relaxation of residual stresses during fatigue cycles in steels. Mater Sci Forum 2003;426-432:3981–6.
[66] Zhuang WZ, Halford GR. Investigation of residual stress relaxation under cyclic load. Int J Fatigue 2001;23:S31–7.
[67] Almer JD, Cohen JB, Moran B. The effects of residual macrostresses and microstresses on fatigue crack initiation. Mater Sci Eng A 2000;284:268–79.
[68] Kobayashi M, Ohno N. Implementation of cyclic plasticity models based on a general form of kinematic hardening. Int J Numer Methods Eng 2002;53(9):2217–38.